

# Structure and zero-dimensional polariton spectrum of natural defects in GaAs/AlAs microcavities

Joanna M Zajac\* and Wolfgang Langbein  
*School of Physics and Astronomy, Cardiff University,  
The Parade, Cardiff CF24 3AA, United Kingdom*

(Dated: October 22, 2018)

We present a correlative study of structural and optical properties of natural defects in planar semiconductor microcavities grown by molecular beam epitaxy, which are showing a localized polariton spectrum as reported in Zajac *et al.*, Phys. Rev. B **85**, 165309 (2012). The three-dimensional spatial structure of the defects was studied using combined focussed ion beam (FIB) and scanning electron microscopy (SEM). We find that the defects originate from a local increase of a GaAs layer thickness. Modulation heights of up to 140 nm for oval defects and 90 nm for round defects are found, while the lateral extension is about  $2\mu\text{m}$  for oval and  $4\mu\text{m}$  for round defects. The GaAs thickness increase is attributed to Ga droplets deposited during growth due to Ga cell spitting. Following the droplet deposition, the thickness modulation expands laterally while reducing its height, yielding oval to round mounds of the interfaces and the surface. With increasing growth temperature, the ellipticity of the mounds is decreasing and their size is increasing. This suggests that the expansion is related to the surface mobility of Ga, which with increasing temperature is increasing and reducing its anisotropy between the [110] and  $[\bar{1}\bar{1}0]$  crystallographic directions. Comprehensive data consisting of surface profiles of defects measured using differential interference contrast (DIC) microscopy, volume information obtained using FIB/SEM, and characterization of the resulting confined polariton spectrum are presented.

## I. INTRODUCTION

Fundamental physics was demonstrated in planar semiconductor microcavities over last 10 years including Bose-Einstein condensation of exciton-polaritons<sup>1</sup>, formation of vortices<sup>2</sup> and superfluidity<sup>3</sup>. To understand these two-dimensional inhomogeneous non-equilibrium systems, it is important to understand and harness spatial disorder in these structures. A significant contribution to polariton disorder in molecular beam epitaxy (MBE) grown microcavities is photonic disorder including a cross-hatched dislocation pattern<sup>4,5</sup> and point-like-defects (PDs)<sup>6</sup>. Such disorder creates a potential landscape for the in-plane motion of polaritons, which results in inhomogeneous broadening, enhanced backscattering<sup>7,8</sup>, and creation of localized polariton condensates and polariton vortices<sup>2,9</sup>.

In this work, we present a correlative study of the structural and optical properties of natural defects in planar semiconductor GaAs/AlAs microcavities grown by MBE. The paper is organized as follows: in Sec. II we review the literature on defects in MBE grown GaAs structures, in Sec. III we discuss the samples and experimental methods used, in Sec. IV we present the experimental results, followed by a discussion of the defect formation in Sec. V and conclusions in Sec. VI.

## II. POINT-LIKE DEFECTS IN GAAS HETEROSTRUCTURES

Point-like-defects observed in MBE-grown GaAs based heterostructures are classified into several types, with the most common being oval defects. It was reported that oval defects originate from an excess of Ga, Ga droplets, or surface contamination<sup>10,11</sup>, or low growth temperatures<sup>12,13</sup>. Oval defects were extensively stud-

ied in the 1990s as they were responsible for the failure of electronic devices such as field-effect transistors.<sup>10</sup> The defects have typical sizes in the order of several  $\mu\text{m}$  and a roughly 3:1 aspect ratio along the  $[\bar{1}\bar{1}0]:[110]$  crystal directions.<sup>11</sup> Their height on the surface were found to be several tens of nanometers. Another type of defect observed in this work were round defects having similar diameters and heights as oval defects. They were attributed<sup>14</sup> to Ga oxide or effusion cell spitting. We found that the defects investigated in our work originate from a GaAs thickness modulation, which we attribute to Ga droplets with sizes in the order of 100 nm emitted by the Ga source during growth. The droplet formation was previously ascribed<sup>10</sup> to an inhomogeneous temperature distribution in the Ga crucible of the effusion cell. Specifically, Ga cools near the orifice of the crucible and, since it does not wet the pyrolytic Boron Nitride (PBN) crucible surface, forms droplets which can fall back into the liquid Ga, causing a spatter of smaller Ga droplets. Recommended methods to reduce this mechanism include 1) use solid instead of liquid Ga; 2) modification of the orifice geometry of the Ga cell to inhibit condensed Ga droplets entering into the Ga source; 3) creating a positive axial temperature gradient toward the orifice to prevent condensation of Ga; 4) treating the crucible with Al, which forms a AlN layer which Ga is wetting, suppressing the formation of droplets. Another mechanism for formation of oval defects is suggested in Ref. 15 and referred to as Ga source spitting. During heating of the Ga source up to 1200°C, within the range of Ga evaporation<sup>16</sup>, explosions in the Ga liquid were observed, which resulted in Gallium droplets deposition on the MBE chamber walls. It was speculated that these explosions were due to  $\text{Ga}_2\text{O}_3$  shells encapsulating Ga and creating an effusion barrier. Another possible mechanism<sup>17</sup> is that particulates released from the walls of the MBE chamber are entering the molten Ga in the crucible causing a turbulent reaction. Summarizing, a number of mechanisms for the

Sample		MC1	MC2
cavity length		$1\lambda_c$	$2\lambda_c$
DBR periods top(bottom)		24(27)	23(26)
growth	DBR AlAs	715	590
temperature	DBR GaAs	660	590
(°C)	cavity GaAs	630	590

TABLE I: Parameters of samples MC1 and MC2.

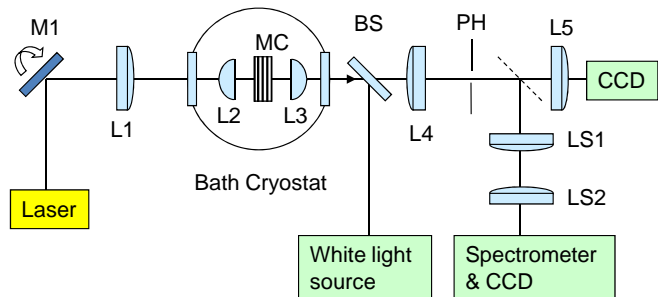


FIG. 1: Sketch of the optical imaging spectroscopy setup used to measure the localized polariton states. M1: Gimbal mounted mirror, L1-L5: Lenses, MC: Microcavity sample, LS1,LS2: movable lenses for imaging, dashed lines: removable mirrors, BS: Beam-splitter.

Ga nano-droplet formation have been suggested, and the mechanism dominant in a given growth is not obvious.

### III. SAMPLES AND EXPERIMENTAL METHODS

In this work we investigated two microcavity samples, MC1 and MC2, grown in a VG Semicon V90 MBE machine with a hot-lip Veeco 'SUMO' cell as Ga source, with structures given in Table I. Sample MC1 was studied in Ref. 6. During the growth of MC1, the wafer temperature was ramped up to 715 °C for the AlAs Bragg layers and down to 660 °C for GaAs Bragg layers, while the cavity layer was grown at 630 °C. During the growth of MC2 instead, the growth temperature was 590 °C for all layers. The two samples show a significantly different aspect ratio of defects on their surface. In MC1 they are essentially round (see Fig. 4), while in MC2 they have an aspect ratio between 3:1 and 2:1 along the  $[1\bar{1}0] : [110]$  direction as shown in Fig. 8. At a temperature of  $T=80$  K, the cavity mode energy in the center of the wafer of MC1 (MC2) is at  $\hbar\omega_c = 1.480(1.431)$  eV, respectively, while the bulk GaAs exciton resonance of the cavity layer is at 1.508 eV.

The low temperature optical measurements were performed using the optical setup sketched in Fig. 1. The samples were mounted strain-free on a mechanical translation stage moving along the sample surface ( $x, y$ ) in a bath cryostat at  $T = 80$  K in nitrogen gas at 100-300 mbar. Two aspheric lenses of 8 mm focal length and 0.5 numerical aperture (NA) were mounted at the opposing faces of the sample inside the cryostat to focus the excitation and collimate the emission, respectively, provid-

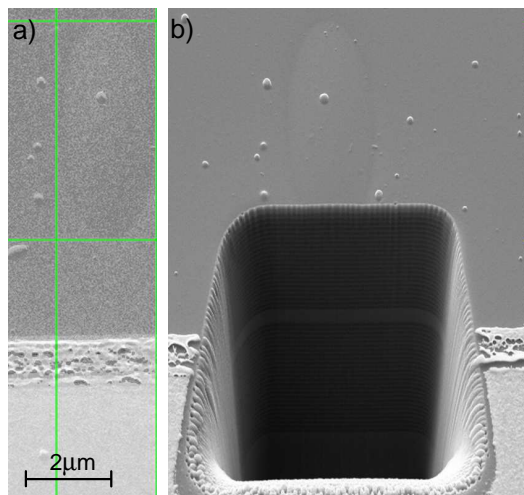


FIG. 2: SEM images of oval defect PD3. a) prior to milling, green lines indicate defect extension on the surface. b) after milling the well exposing the epilayer cross-section at its side wall. On the lower part of the images, the edge of the alignment photomask is visible.

ing a diffraction limited resolution of 1  $\mu\text{m}$ . The axial positions of both lenses were adjustable at low temperatures to control the focus of excitation and detection. The excitation was provided by a mode-locked Ti:Sapphire laser (Coherent Mira) delivering 100 fs pulses at 76 MHz repetition rate and a spectral width of approximately 20 meV. The transmission of the samples excited from the substrate side and detected from the epi-side was imaged onto the input slit of an imaging spectrometer with a spectral resolution of 15  $\mu\text{eV}$ . Scanning of the sample image across the spectrometer input slit while keeping the directional image on the spectrometer grating fixed for two-dimensional hyperspectral imaging was achieved by moving the lenses LS1 and LS2 appropriately<sup>18</sup>.

Spatial height profiles of defects on the sample surface were measured with differential interference contrast (DIC) microscopy using an Olympus BX-50 microscope with a 20x 0.5NA objective. DIC images in green light (wavelength range 525-565 nm) were taken by a Canon EOS 500D camera with an array of 4752 x 3168 pixels of 4.8  $\mu\text{m}$  size in the intermediate image plane. The resulting image resolution was 650 nm in the plane of the sample, and about 2 nm in the plane perpendicular to the sample surface using quantitative DIC. Details on the procedure used to extract height profiles of defects using DIC microscopy are given in the Appendix.

To investigate the sample structure below the surface, we used a Carl Zeiss XB1540 Cross-Beam focussed-ion-beam (FIB) microscope which combines an ion-beam milling/imaging column with field-emission scanning electron microscope (FESEM)<sup>19</sup>, providing an imaging resolution of about 50 nm for the samples studied. The internal epi-layer structure was exposed by FIB milling. Smooth cross-sections were obtained using a two stage milling procedure. In the first step, a high beam current of 2 nA, was used, resulting in fast milling but leaving a rough and inhomogeneous interface due to sputtering and redeposition of material. In the second

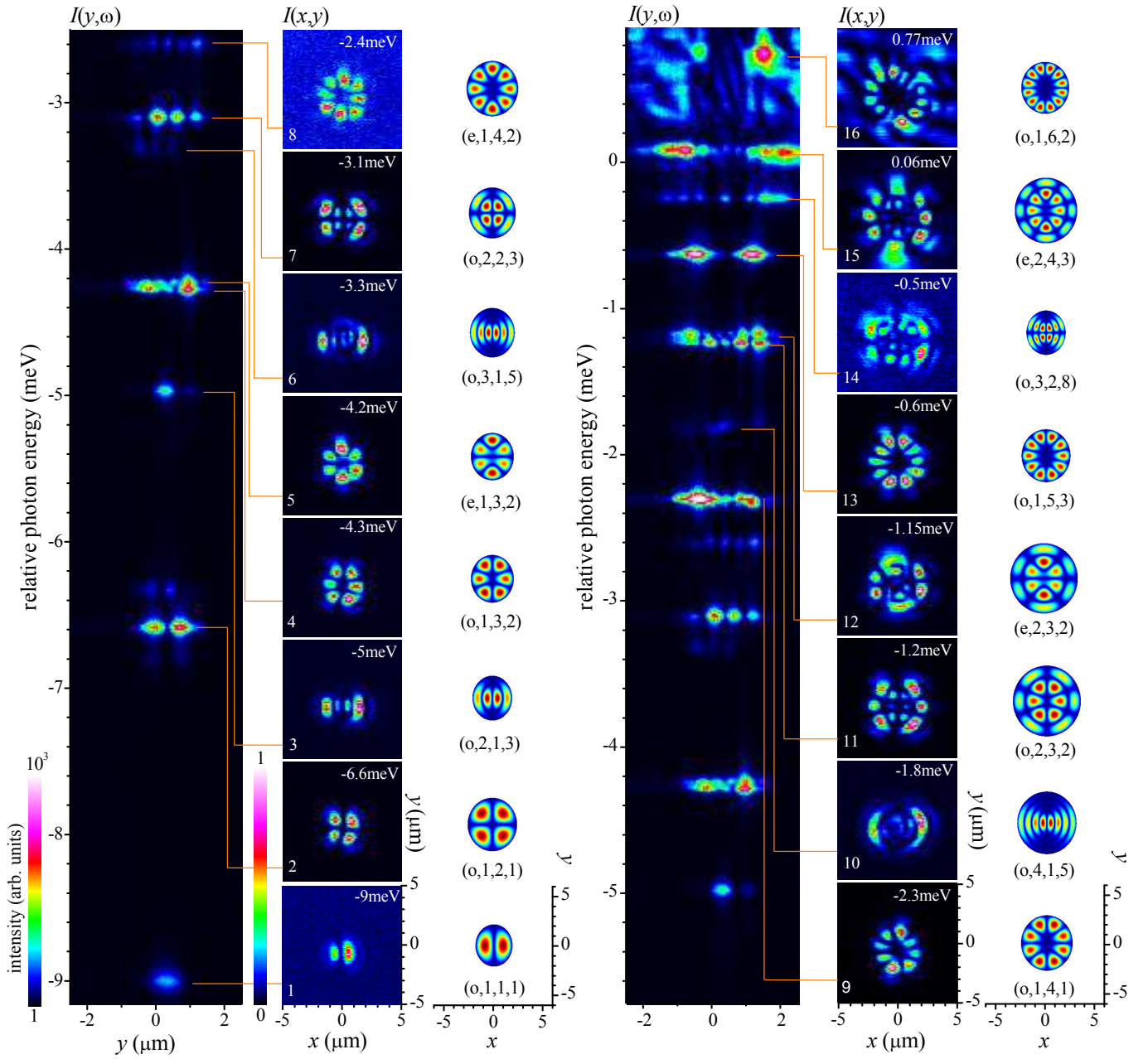


FIG. 3: Hyperspectral imaging of polariton states bound to PD1 in MC1, measuring the spatially and spectrally resolved transmission intensity  $I(x, y, \omega)$ . First and fourth column:  $I(0, y, \omega)$ . The energy is shown relative to the polariton band edge at  $\hbar\omega_c = 1.4789\text{eV}$ . Intensity on a logarithmic color scale as indicated. Second and fifth column: Real space intensity maps of individual states  $I(x, y, \omega_l)$ . The state number  $l$  and the relative energy  $\hbar(\omega_l - \omega_c)$  are given, and the orange lines indicate the related peaks in  $I(0, y, \omega)$ . Third and sixth column: Real space distributions  $|\Psi_{n,m,q}|^2$  of corresponding Mathieu functions, labeled by their parity ('e': even, 'o': odd), radial ( $n$ ) and angular ( $m$ ) order, and parameter  $q$  (see Eq.(1) and Eq.(2)). Color scale as for measured data indicated in the first column.

step, the surface was polished with a lower beam current of 200 pA removing a layer of about 500 nm per cut resulting in a negligible surface roughness. In the next steps, layers with a thickness of  $1\mu\text{m}$  or less were removed using the low beam current. Different stages of this milling procedure are shown in Fig. 2. Before milling, the oval defect (PD3) is seen in SEM (Fig. 2a), with the vertical image scale corrected for the viewing angle of  $36^\circ$  to the sample surface. A rectangular well of about  $14\mu\text{m}$  width and  $7\mu\text{m}$  depth is milled into the surface to

one side of the defect (Fig. 2b), exposing a cross-section through the epi-layers to be measured at its side walls. After imaging the exposed cross-section with SEM, the subsequent cross-section at a controlled distance further into the structure is milled. Steps sizes of about  $1\mu\text{m}$  were used at the outskirts of the defect, reducing down to  $100\text{nm}$  at its center to resolve the defect source. The cross-sections were  $6-7\mu\text{m}$  deep to expose the complete epitaxial structure, and their width was adjusted to the lateral extension of the defect observed at the surface. In

order to mark defects on the sample surface for the correlative studies, a gold alignment mask was fabricated on the surface by photolithography. The mask consisted of a grid of  $400\ \mu\text{m} \times 400\ \mu\text{m}$  squares with column and row indexing. Considering the defect density in the order of  $10^3/\text{cm}^2$ , this mask allows to trace individual defects through the different measurement techniques used in the present investigation.

## IV. RESULTS

### A. Sample MC1

The localized polariton states in the round defects of sample MC1 were examined previously in Ref. 6. Here we report on the correlation between the states and the three-dimensional structure of these defects using two defects referred to as PD1 and PD2 as examples. The localized polariton states of PD1 are observed in the hyperspectral transmission images shown in Fig. 3. The defect shows 16 localized modes down to  $-9\ \text{meV}$  below the polariton band edge. It can be noted that the lowest observed state is of  $p_x$ -type symmetry. We expect to have 2 states with lower energies, another  $p_y$ -state and an  $s$ -state. These were not recorded.

To qualitatively understand the states bound to this defect, we compare them with solutions of the two-dimensional time-dependent wave equation  $(\partial_x^2 + \partial_y^2 - \partial_t^2/v^2)\Psi = 0$  with the velocity  $v$  for elliptical boundary conditions. Using elliptical coordinates  $x = c \cosh(\xi) \cos(\eta)$ ,  $y = c \sinh(\xi) \sin(\eta)$  with the focus distance  $c$ , and the ansatz  $\Psi(x, y, t) = R(\xi)\Phi(\eta)e^{i\omega t}$  results in the ordinary and modified Mathieu equations for the angular part  $\Phi(\xi)$  and radial part  $R(\xi)$ , respectively:<sup>20</sup>

$$(\partial_\eta^2 + \lambda - 2q \cos(2\eta))\Phi = 0 \quad (1)$$

$$(\partial_\xi^2 + \lambda - 2q \cosh(2\eta))R = 0 \quad (2)$$

where  $q = (\omega c/2v)^2$  is the square of the normalized frequency. The solutions of  $\Phi$  and  $R$  are angular and radial Mathieu functions. For a given  $q$ , the periodic boundary condition of the angular part  $\Phi$  in Eq.(1) determines a series of  $\lambda_m(q)$  with ascending number of nodes  $m = 0, 1, 2, \dots$ , each of which except  $m = 0$  is a doublet, having an odd (o) or even (e) symmetry for inversion of  $y$ . The elliptical boundary is given by a unique  $c$  and  $\xi_0$ , at which the boundary condition, for example  $R(\xi_0) = 0$ , holds. This condition and Eq.(2) using  $\lambda = \lambda_m(q)$  determines the mode frequencies  $q_{n,m}$  corresponding to modes with ascending number of nodes  $n = 0, 1, 2, \dots$  in radial direction. Analytic expressions for the solutions are given in Ref. 21.

Since the polaritons show a quadratic in-plane dispersion for small wavevectors, their in-plane motion is well described by the Schrödinger equation.<sup>22</sup> By modifying the definition of  $q$ , the above solutions for the Helmholtz equation are also solving the Schrödinger equation for elliptical boundary conditions, such as the elliptical quantum well with infinite barriers.<sup>23</sup>

Another family of analytic solutions of the Schrödinger equation with elliptical symmetry are given by

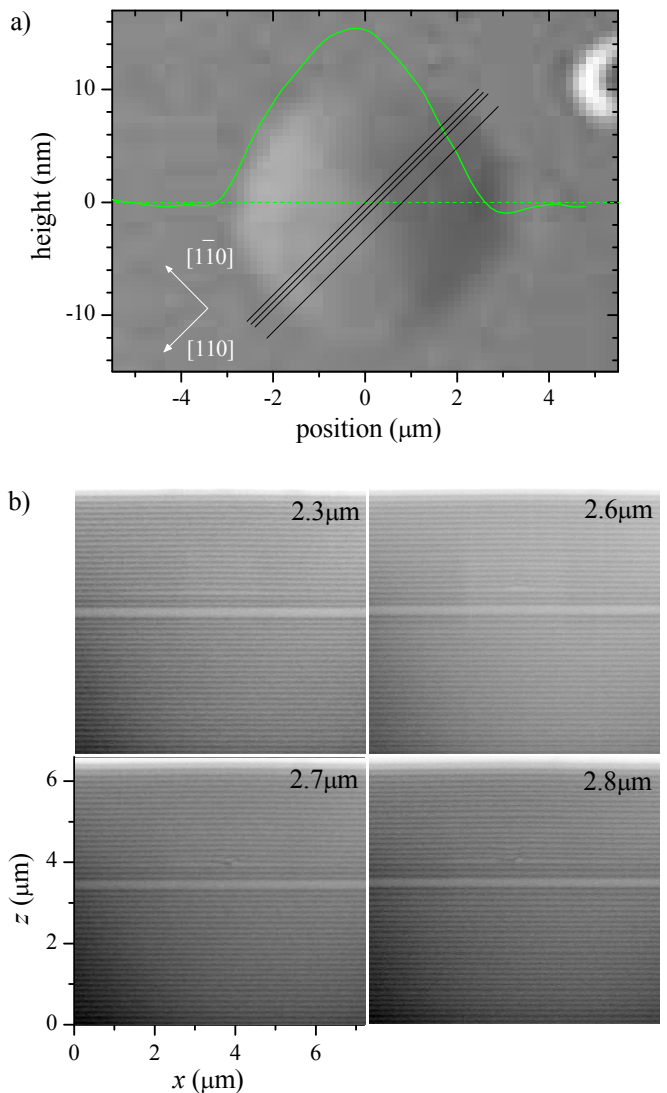


FIG. 4: Structural characterization of PD1. a) DIC image of the sample surface (linear grey scale) and resulting height profile across the defect center (green line). b) SEM images of cross-sections through the epitaxial structure, taken along the black lines indicated in a). The relative distances from the edge of the defect are indicated.

the Hermite-Gaussian modes of an anisotropic two-dimensional harmonic oscillator. However, we found that they do not describe the observed distributions well, since, as we will see later, the confining potential of PD1 is not similar to a parabolic potential but rather to an elliptical well.

The solutions<sup>24</sup>  $|\Psi_{n,m,q}|^2$  with the mode orders  $n, m$  assigned to the measured states of intensities  $|\psi_l|^2$  are shown in Fig. 3, yielding a qualitative agreement. For each energy state,  $q$  was adjusted in order to reproduce the experimental patterns.

The structural characterization of PD1 by DIC and FIB/SEM is given in Fig. 4. The DIC data shows a diameter of the defect on the surface of about  $6\ \mu\text{m}$ , similar to the extension of the spatially resolved transmission from this defect, and a height up to about  $15\ \text{nm}$ . The FIB/SEM cross-sections show the origin of the defect -



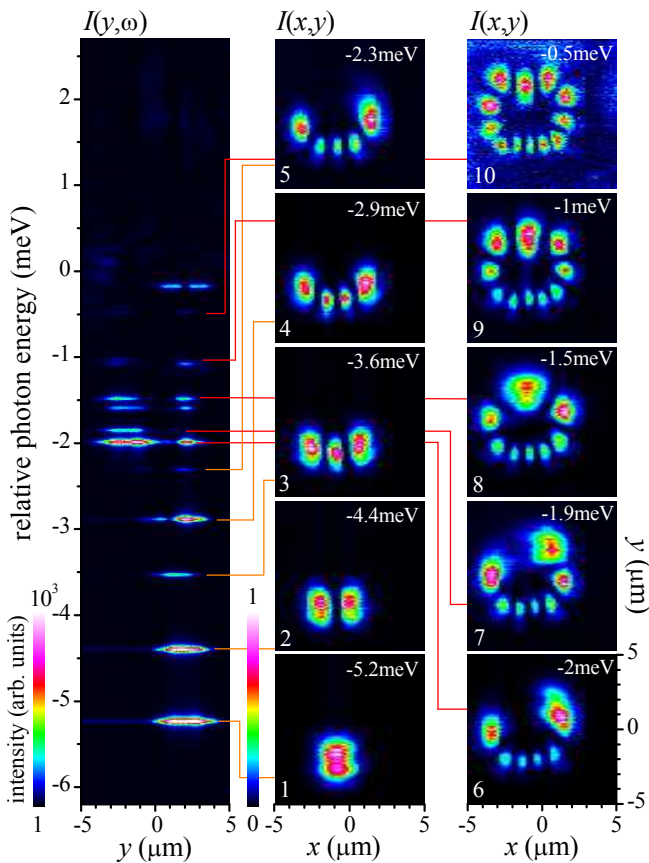


FIG. 5: Hyperspectral imaging of polariton states bound to PD2 in MC1 with  $\hbar\omega_c = 1.4787$  eV, detailed description as for Fig. 3.

a thickened GaAs layer with a center depression in the third DBR period above the cavity, extending over  $4 \mu\text{m}$  in  $x$ , and adding about  $60$  nm in thickness in the center, visible in the  $y = 4.5 \mu\text{m}$  cross-section. Further discussion of the defect growth dynamics will be given later.

We now move to the second defect PD2 on MC1, for which the hyperspectral transmission images are shown in Fig. 5. The states are arranged along a ring of about  $6 \mu\text{m}$  diameter, with the lowest state localized at small  $y$ , and higher states gradually extending along the ring, as in a one-dimensional harmonic oscillator, until the whole ring is filled. The underlying potential for the polaritons appears to be a ring-shaped well, with a depth decreasing with increasing  $y$ . The analysis of the potential from the states shown in Sec. IV C confirms this interpretation.

The structural characterization of PD2 by DIC and FIB/SEM is given in Fig. 6. The surface profile is similar to PD1, with a size of about  $7 \mu\text{m}$  diameter. The defect source is much deeper in the structure than for PD1, in the 23rd period of the DBR below the cavity, and has a larger height of about  $90$  nm. This height is about twice the nominal height of the GaAs  $\lambda_c/4$  layer, and leads to discontinuities of the DBRs for about 4 layers above the defect. The deep center depression of the defect is consistent with the ring-shaped polariton confinement potential shown in Fig. 11.

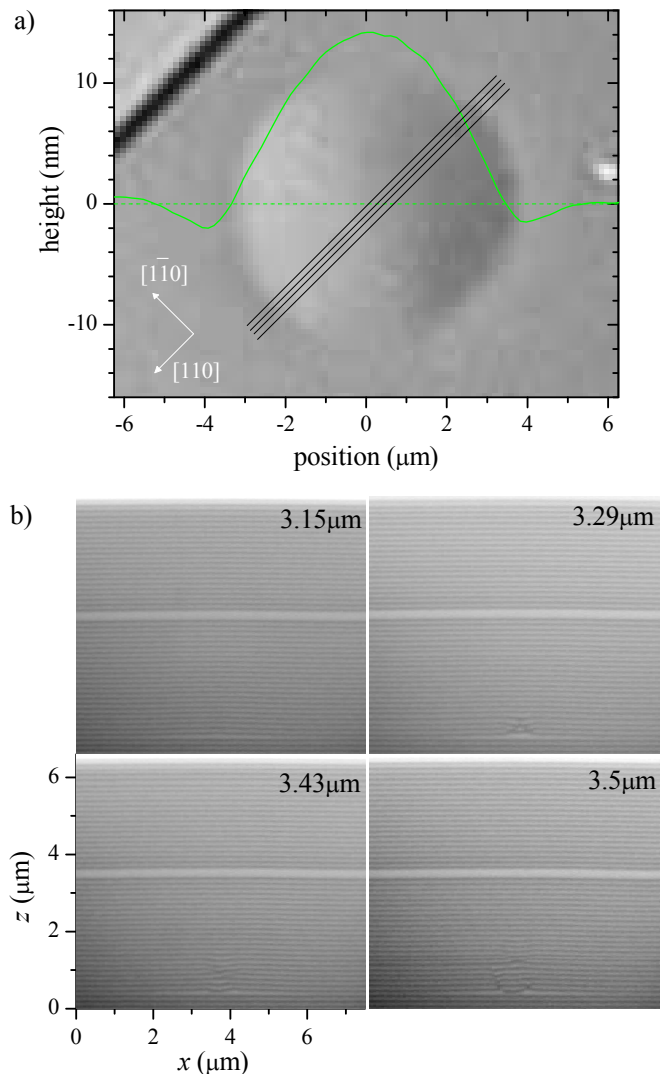


FIG. 6: Structural characterization of PD2, detailed description as for Fig. 4.

## B. Sample MC2

This sample was grown at lower temperature than MC1 (see Table I), and shows oval-shaped defects. Two examples of defects for this samples are given here, referred to as PD3 and PD4. The polariton states of PD3 are visible in the hyperspectral transmission images in Fig. 7. The states come in nearly degenerate pairs with point reflected wavefunctions, extended along the  $x$ -axis ( $[1\bar{1}0]$ ), for example the state pairs (1,2) and (3,4), (5,6). The states also have an approximate mirror symmetry about the  $x$  axis. Similar "double-well" eigenstates were observed for several other oval defects in this sample. All of them exhibit the same sequence of states, while the number of confined states was varying.

Localization of the states close to the center of the defect, and the absence of mixed states of different parities indicate a very high potential barrier in the middle, and deep wells on both sides, with the corresponding potential in  $y$  direction could be written as  $V(y) \propto \delta(y/b) + a/(|y/b| + 1)$  with the scaling constants  $a, b$ . The

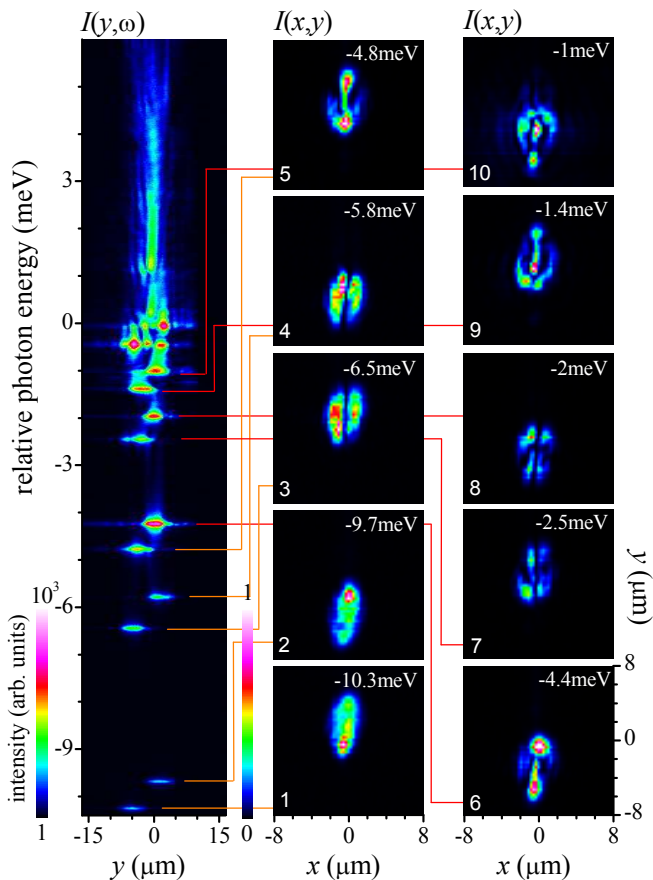


FIG. 7: Polariton spectrum of PD3 with  $\hbar\omega_c = 1.4353$  eV, detailed description as for Fig. 3.

resulting states of the two sides  $y \lesseqgtr 0$  do not mix significantly. The states for  $y < 0$  are shifted by  $< 1$  meV to higher energies. In both wells we observe a ground state, followed by the first excited state some 4 meV above having one node and the second excited state some 2 meV further having two nodes, the third excited state some 2 meV with 3 nodes, and higher states.

The structural characterization of PD3 is given in Fig. 8. The surface profile is oval, with the extension along  $[110]$  of  $3 \mu\text{m}$ , reduced by a factor of two compared to the one of PD1, while the extension along  $[\bar{1}\bar{1}0]$  of  $6 \mu\text{m}$  is similar to one of PD1. The height of the surface modulation is about 140 nm, twice the value seen for PD1 and PD2, and about twice the nominal height of the GaAs Bragg layer. The height increase is consistent with the reduced lateral size when accommodating the same volume. The defect source is in the 20th DBR period below the cavity.

We now move to the second defect PD4 on MC2, for which the hyperspectral transmission images are given in Fig. 9. It shows the deepest localized states of all PDs studied, with the ground state 40 meV below the continuum. The states show an approximate mirror symmetry along the  $x$  and  $y$  axis. We can model them with Mathieu functions as shown in Fig. 9, using a strong ellipticity. The structural characterization of PD4 is given in Fig. 10. The surface profile is oval as PD3, but with a 20% smaller extension and a three time smaller height. The defect

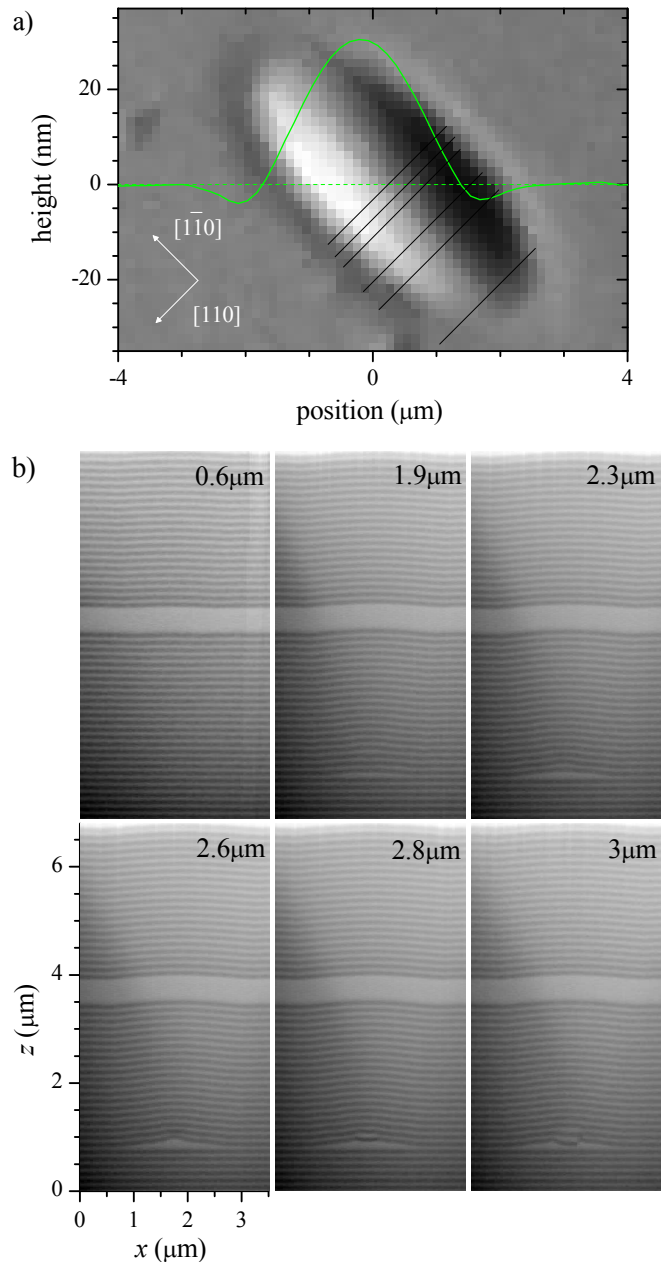


FIG. 8: Structural characterization of PD3, detailed description as for as Fig. 4.

source is in second period of the DBR below the cavity, and has a height of about 100 nm. Being so close to the cavity, the additional GaAs has a strong influence on the polariton states, and the crater in the middle gives rise to a confinement potential with a barrier between the center and the peripheral area, as evidenced by the spatial distribution of the confined wavefunctions.

### C. Potential Reconstruction

The observed localized polariton states can be related to an effective confinement potential  $V_m(\mathbf{r})$  for the in-plane polariton motion. We can estimate  $V_m(\mathbf{r})$  using the spectrally integrated density of states  $D_m(\mathbf{r})$  created by

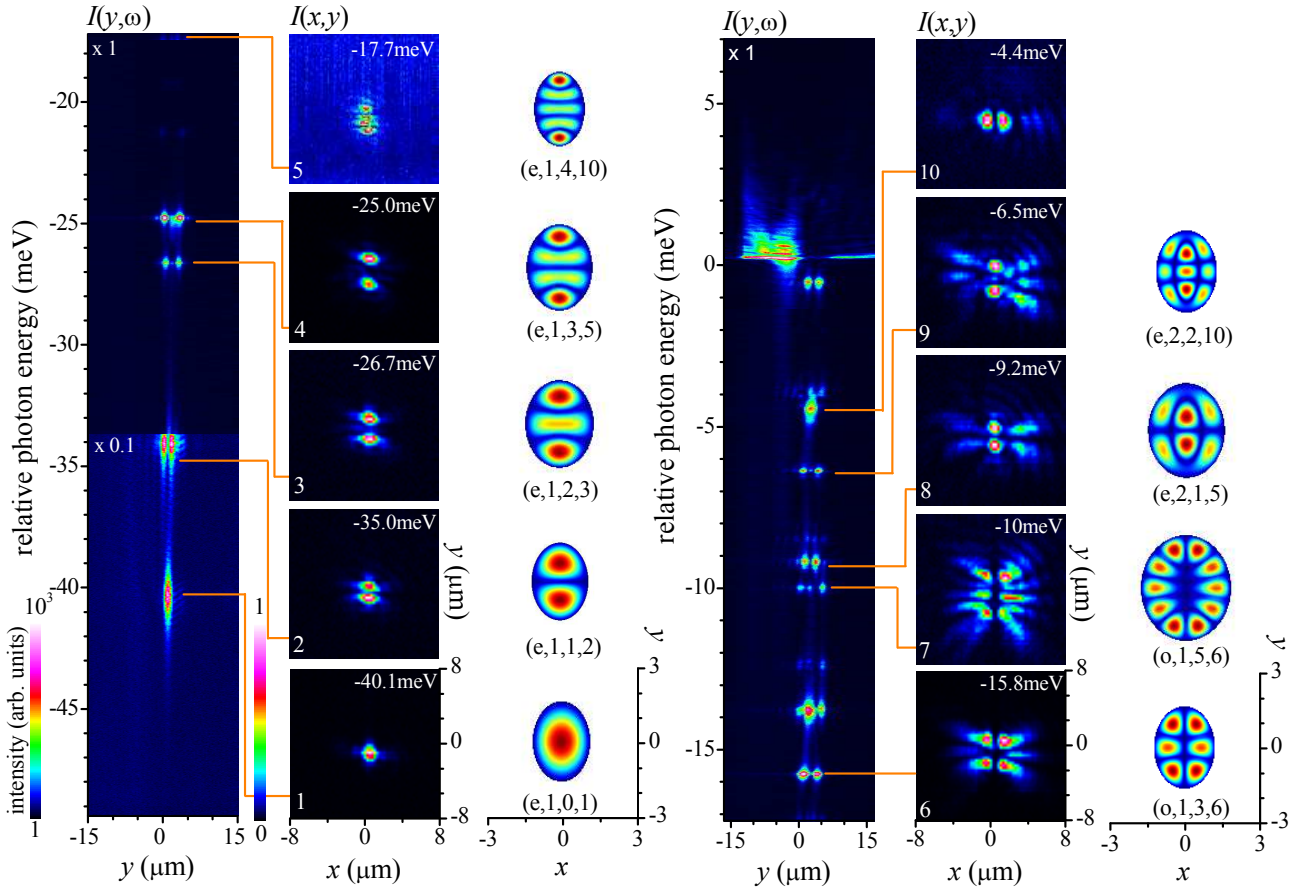


FIG. 9: Polariton spectrum of PD 4 with  $\hbar\omega_c = 1.4343$  eV, detailed description as for Fig. 3.

$V_m(\mathbf{r})$  below the continuum edge as introduced in Ref. 6. We use

$$D_m(\mathbf{r}) = \sum_{n=1}^{n_m} |\Psi_n(\mathbf{r})|^2 \quad (3)$$

where the bound state probability densities  $|\Psi_n(\mathbf{r})|^2$  are taken as the normalized measured intensities

$$|\Psi_n(\mathbf{r})|^2 = \frac{I(\mathbf{r}, \omega_n)}{\int I(\mathbf{r}, \omega_n) d\mathbf{r}^2}. \quad (4)$$

This expression assumes that the emitted field is proportional to the polariton wavefunction, which is valid for a cavity lifetime which is constant for the in-plane wavevector components of the bound states. This is a good approximation for small in-plane wavevectors, less than 10% of the light wavevector in the cavity of about  $26/\mu\text{m}$ . Some of the strongly localized states in our study with small feature sizes are likely to deviate from this approximation.  $D_m(\mathbf{r})$  is given by the integral of the free density of states from zero kinetic energy at the potential floor to the continuum when neglecting the spatial variation of the confinement potential, *i.e.* in the limit of small level splitting compared to the confinement potential. In two dimensions the density of states is constant and given by  $D_{2D} = m/(2\pi\hbar^2)$ , and we find  $V_m(\mathbf{r}) = -D(\mathbf{r})/D_{2D}$ . We use the effective mass of the polaritons from the measured dispersion  $m = 2 \cdot 10^{-5} m_e$ , where  $m_e$  is the free

electron mass. The resulting confinement potentials for the investigated PDs are shown in Fig. 11. The symmetry of the potentials reflect the symmetry of the localized states.

#### D. Surface Reconstruction

The series of SEM cross-section images  $S(x, y_n, z)$  taken at various  $y_n$  (see Figs. 4, 6, 8, 10), provide volume information of the defects. To reconstruct the shape of the defects in three dimensions, we determine the position of the interfaces between the GaAs and AlAs layers in the SEM image. We use PD3 (see Fig.8) as an example here. The SEM images show a signal  $S$ , which is proportional to the detected secondary electron current, differing by about 10% between AlAs and GaAs surfaces. The RMS noise in  $S$  was about 5% of the GaAs signal. SEM images were taken with a nominal magnification between 65600 and 79500. We calibrated the vertical ( $y$ ) axis to match the nominal Bragg period, yielding pixel sizes between 10 nm and 12 nm with 2% error. The noise of  $S$  is limiting the precision with which the layer interface positions can be determined. To enable a reliable fit of the interface positions, we have averaged the data over 5 pixels (60 nm) along  $x$ , orthogonal to the growth direction  $z$ . The resulting  $\bar{S}(x, y_n, z)$  was fitted with a model function  $S_m(z)$  of the epitaxial structure along  $z$ .

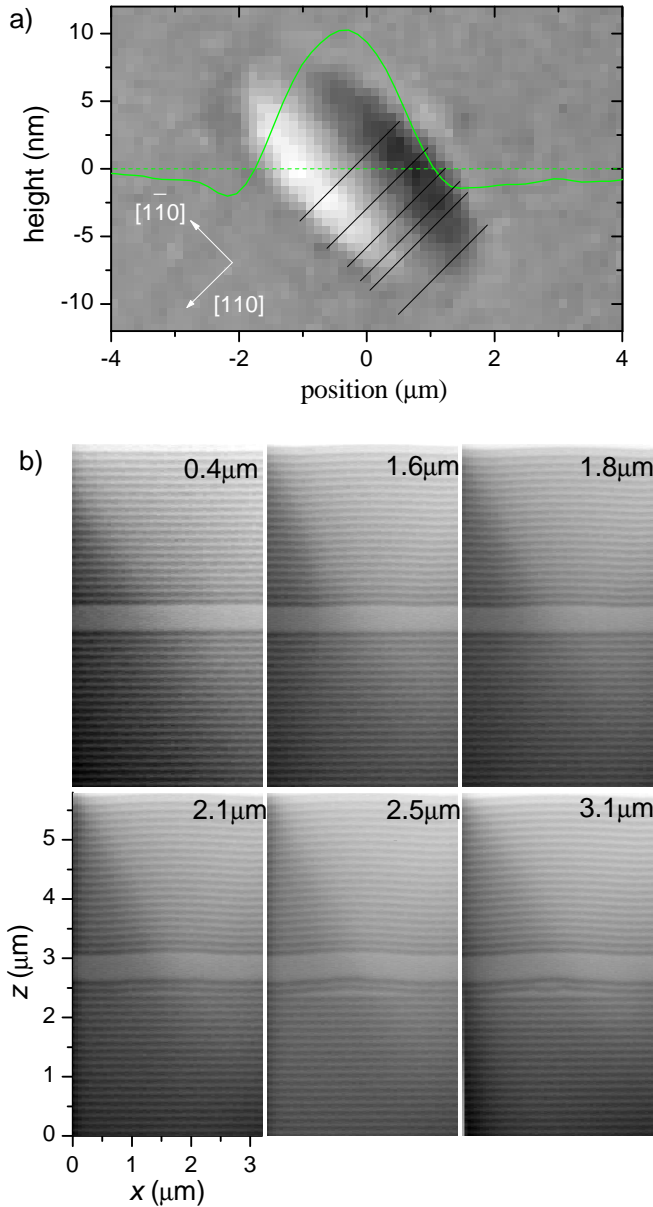


FIG. 10: Structural characterization of PD 4, detailed description as for as Fig. 4.

The model assumes a Gaussian resolution of the imaging with a variance of  $r/\sqrt{2}$ , and a constant thickness  $d$  of the  $\lambda_c/4$  AlAs layers, not affected by the defect, which is motivated by the small surface diffusion length of AlAs compared to GaAs. The sequence of  $L$  AlAs layers in GaAs is then described by

$$S_m(z) = a_0 + a_1 z + a_2 z^2 + A \times \sum_{l=1}^L \left[ \operatorname{erf} \left( \frac{z - z_l}{r} \right) - \operatorname{erf} \left( \frac{z - z_l - d}{r} \right) \right]. \quad (5)$$

The polynomial coefficients  $a_{0,1,2}$  describe the background,  $A$  is half the signal difference between AlAs and GaAs, and  $z_l$  are the positions of the lower interfaces of the AlAs layers. The layer index  $l$  is the AlAs layer number in growth direction. The topmost 3-4 layers were excluded from the fitted region as the background varied

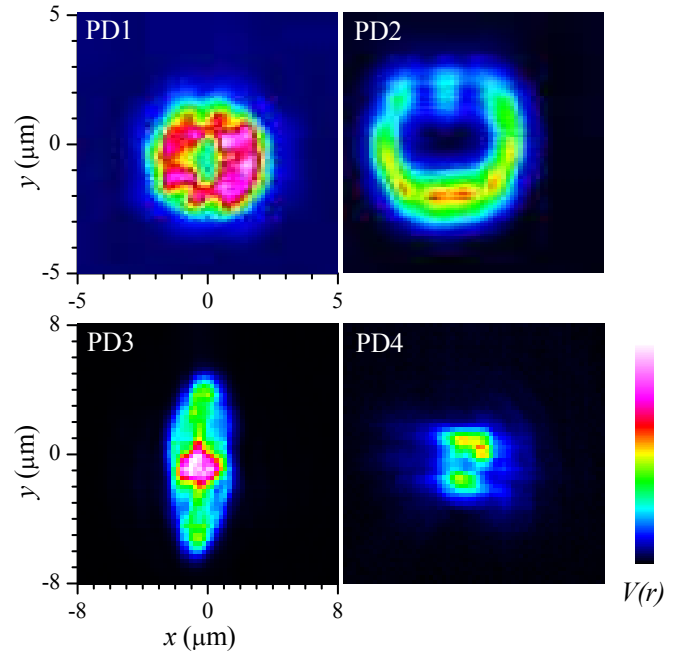


FIG. 11: Potentials  $V_m(\mathbf{r})$  of PDs calculated using Eq.(4). The color scale is given, covering 0 to -24 meV for PD1 and PD2 and 0 to -46 meV for PD3 and PD4.

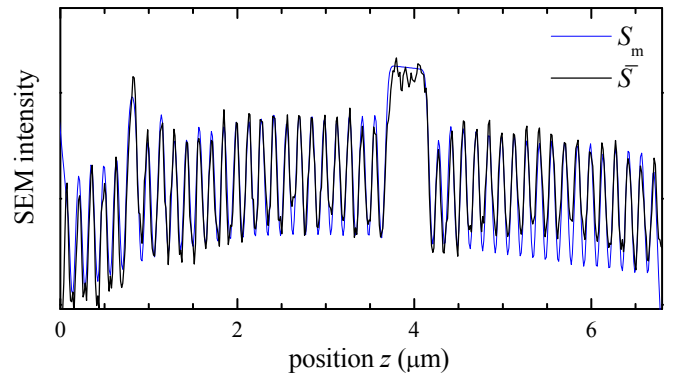


FIG. 12: Example of a fit (blue line)  $S_m(z)$  to the SEM profile  $\bar{S}(z)$  (black line) of PD3, position  $(x, y_n) = (1.5 \mu\text{m}, 2.5 \mu\text{m})$  in Fig. 8. A linear offset has been subtracted for better visibility.

strongly due to the change in secondary electron collection efficiency (see *e.g.* Fig. 4b). The resolution parameter  $r$  was 40 nm corresponding to a FWHM of 67 nm. The fitted layer positions  $z_l$  show a noise of a few nm. An example of such a fit is given in Fig. 12. Using the  $z_l(x, y_n)$  for the different cross-sections  $n$ , we can reconstruct height maps of the AlAs layers within the structure across  $x$  and  $y$ . A linear slope and an offset along  $x$  were subtracted from each  $z_l(x, y_n)$  of an individual cross-section  $n$  to reproduce the nominal position outside the defect.

The height maps of PD3 reconstructed from 15 cross-sections (see lines in Fig. 8, not all shown) are displayed in Fig. 13. The evolution of the surface modulation can be followed. The first layer above the defect source ( $l = 7$ ) shows the center depression of the GaAs, similar to what observed in liquid droplet epitaxy<sup>25</sup>. Two maxima of the



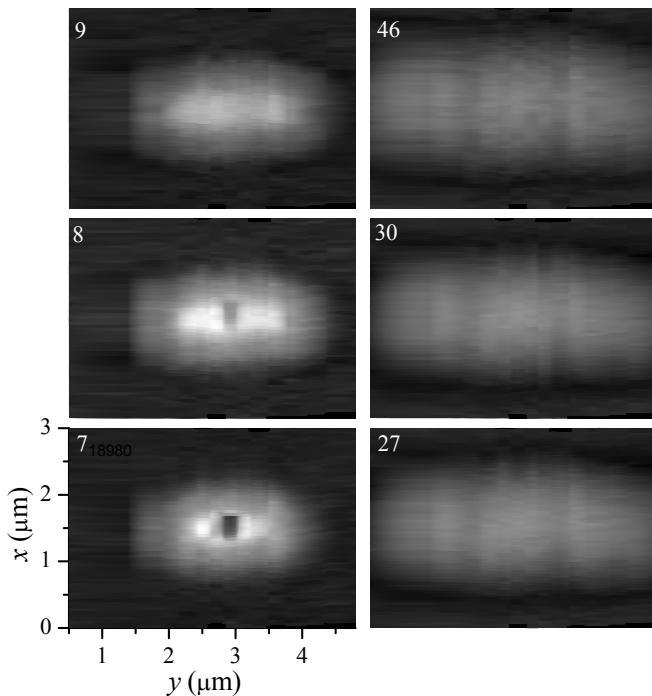


FIG. 13: Height maps of AlAs layers in PD3. The sequential numbers of the layers  $n$  are given. Linear grey scale from  $-20$  nm (black) and  $+140$  nm (white) relative to the nominal layer position. The layer 7 is the first above the GaAs layer containing the droplet, layer 27 is the first layer above the  $2\lambda$  GaAs cavity layer, and layer 46 is the last fitted layer.

thickness are observed along the preferential surface diffusion direction  $[1\bar{1}0]$ . With increasing layer number, first the depression disappears ( $l = 9$ ), followed by a general extension and flattening of the structure. By integrating height profiles of defect for different cuts we have determined the volume of the additional GaAs material as constant within the error. From this volume, we can deduce the radius of the deposited Ga droplet which is  $86 \pm 6$  nm.

## V. DISCUSSION

For all of the 15 PDs investigated in this work, of which four have been shown as examples, we find a similar origin - a local increase in a GaAs layer thickness with a depression in the center. The additional GaAs volume can only be created by a local deposition of Ga, as the growth is limited by the group III element, while the group V element As is provided in a much larger amount given by the V/III flux ratio of about 50, and desorbs if not bound to the surface with a Ga atom to form GaAs. The only available source for this excess Ga deposition are Ga droplets from the Ga source.

The shapes of the polariton potentials created by the PD are a consequence of the Ga droplet size, and its deposition position relative to the cavity layer. In order to simulate the 0-dimensional polariton states quantitatively, a full three-dimensional simulation of the mode structure in the cavity would be needed, which is be-

yond the scope of the present work. For a qualitative argument, one can use a first-order perturbation picture. The polariton intensity is decaying exponentially into the Bragg mirror with a decay length of about 400 nm. For PD2, the GaAs layer thickening is 50 nm, but it is separated by 23 DBR periods, about  $3 \mu\text{m}$ , or 8 decay lengths from the cavity, where the polariton intensity has decayed to 0.02%. This results in a small influence to the polaritons and a small localization energy of the ground state of 5 meV. For this defect we observe a large central crater and DBR layer discontinuities, as can be seen on the central cut in Fig. 4. This could give rise to a repulsive central part of the PD2 potential as observed in Fig. 11.

In PD1, the Ga droplet had a similar size as in PD2 (GaAs thickening 90 nm), but it hit the surface only three DBR periods above the cavity layer. Even though the induced structural perturbation propagates away from the cavity layer, it has a much larger influence, with the third excited state at  $-9$  meV and an estimated ground state confinement energy of 20 meV. The significantly smaller lateral extension of the defects in MC2 leads to a larger height of the perturbation, which in turn results in stronger confinement of polariton states with shapes as seen for PD3 and PD4.

The evolution of the defect structure during growth can be pictured as follows. After a Ga droplet was deposited on the surface, Ga diffuses over the surface from the droplet to the surrounding areas. Due the large V-III flux ratio, there is sufficient surplus of  $\text{As}_2$  impinging onto the surface to convert the diffusing Ga into GaAs, leading to an additional GaAs thickness which decays with the distance from the deposition spot, according to the Ga diffusion length. The depression in the center of the resulting profile is due to reduced GaAs growth below the Ga droplet, which requires the diffusion of As through the Ga droplet to the GaAs surface. Once the droplet has been consumed, the subsequent GaAs growth generally tends to smooth the surface due to the Ga surface diffusion and the preferential attachment of Ga at monolayer steps, which have a density proportional to the surface gradient for gradients superseding the gradient due to monolayer islands (for a island size of 20 nm a gradient of 1%). Al instead has a much shorter diffusion length, and therefore the surface profile is essentially conserved during the growth of the AlAs layers. For Ga grown on (001) oriented substrate at  $590^\circ\text{C}$  at a V/III flux ratio of 2 and a growth rate of  $0.25 \mu\text{m}/\text{h}$  the diffusion length was reported<sup>26</sup> to be  $1 \mu\text{m}$  and  $0.02 \mu\text{m}$  for Ga and Al, respectively.

The observed PD anisotropy of 1:2 to 1:3 along the  $[110]:[1\bar{1}0]$  directions for MC2 grown at a temperature of  $590^\circ\text{C}$  reduces to less than 1:1.1 for MC1 grown at  $715^\circ\text{C}$ . This finding can be explained by temperature dependent diffusion lengths  $D$  for these two crystallographic directions. In Ref. 27  $D_{[1\bar{1}0]} = 4D_{[110]}$  was found resulting in diffusion lengths of  $L_{[1\bar{1}0]} = 2L_{[110]}$  for a V/III flux ratio of 1.5 and growth temperatures in the range of  $600^\circ\text{C}$ , in agreement with the aspect ratio of the defects found in MC2. The reduction of the anisotropy for the higher growth temperature of MC1 indicates an ac-

tivated diffusion with different activation energies in the two directions. At higher temperatures, the thermal energy supersedes the activation energies and a kinetically limited isotropic diffusion is recovered. The presence of different activation energies for diffusion in the two crystallographic directions is plausible as during growth the GaAs surface shows a reconstruction<sup>28</sup> giving rise to a channel-like structure along  $[1\bar{1}0]$ .

## VI. CONCLUSIONS

We have shown that oval or round defects in MBE grown GaAs microcavities create zero-dimensional polariton states of narrow linewidths. We have revealed their three-dimensional structure and their formation mechanism, an impinging Ga droplet during growth. While we have deduced effective confinement potentials for the defects, a quantitative modeling of the polariton spectra from the three-dimensional structural information obtained by the FIB/SEM data is presently missing. In the context of polaritonic devices,<sup>29</sup> our work indicates an approach to manufacture two-dimensional polaritonic traps by intentional creation of Ga droplets at a specific position during the MBE growth of a microcavity, rather than ex-situ etching as described in Ref. 30. One could also use Ga droplet epitaxy<sup>31</sup> with a low density to create well-defined localized polariton states in microcavities. The narrow linewidths of the polariton states formed in this way are favorable for zero-dimensional polariton switches.<sup>32</sup>

## VII. ACKNOWLEDGMENTS

The samples were grown at the EPSRC National Centre for III-V Technologies, Sheffield, UK, by Maxime Hugues and Mark Hopkinson (MC1), and Edmund Clarke (MC2). The FIB/SEM investigations were conducted at the London Centre for Nanotechnology, and funded by the EPSRC Access to Materials Research Equipment Initiative under grant EP/F019564/1. We thank Suguo Huo and Paul Warburton for training and assistance with the FIB/SEM. We acknowledge discussions with Paola Atkinson and Edmund Clarke on the growth kinetics, and help with the photolithography by Phil Buckle and Karen Barnett. This work was supported by the EPSRC under grant n. EP/F027958/1.

## VIII. APPENDIX

### A. Quantitative Differential Interference Contrast Microscopy

Differential interference contrast microscopy (DIC), also known as Nomarski microscopy, was used in reflection in this experiment. A Nomarski prism assembly (DIC Slider U-DICT with Polarizer U-ANT) is mounted in a Olympus BX-50 upright microscope. The illumination from a mercury arc lamp is split by the Normarski prism

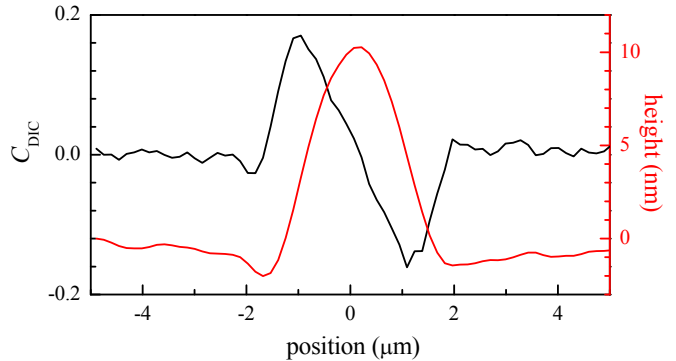


FIG. 14: DIC contrast  $C_{\text{DIC}}$  (black line) as function of the sample position  $s$  along the shear direction, and resulting height profile  $h$  (red line) calculated using Eq.(8).

into two beams 1,2 shifted by the shear displacement  $\Delta$  in the object plane, with linear polarizations along and orthogonal to  $\Delta$ . The reflected beams are recombined by the prism, creating a polarization state depending on their relative phase  $\varphi_1 - \varphi_2$ . The transmission through the polarizer depends on the polarization state, such that the intensity depends on the relative phase in the way

$$2I_{\text{DIC}} = I(1 - \cos(\phi_o + \varphi_1 - \varphi_2)) \quad (6)$$

where the offset phase  $\phi_o$  is introduced by an adjustable spatial offset of the Normarski prism along the optical axis from its nominal position for which the beams are not displaced in the directional space (objective back focal plane). The shear  $\Delta$  is similar to the optical resolution of the microscope objective, which allows to approximate the phase difference between the two beams in first order as the shear times the phase gradient at the observed position,  $\varphi_1 - \varphi_2 \approx \Delta \cdot \nabla \varphi$ , such that Eq.(6) can be written as  $2I_{\text{DIC}} = I(1 - \cos(\phi_o + \Delta \cdot \nabla \varphi))$ . Choosing  $\phi_o = \pm\pi/2$ , and developing up to first order in the phase difference, we get  $2I_{\text{DIC}}^{\pm} = I(1 \pm \Delta \cdot \nabla \varphi)$ . Measuring  $I_{\text{DIC}}$  for both offset phases, we determine the contrast

$$C_{\text{DIC}} = \frac{I_{\text{DIC}}^+ - I_{\text{DIC}}^-}{I_{\text{DIC}}^+ + I_{\text{DIC}}^-} = \Delta \cdot \nabla \varphi \quad (7)$$

We can now integrate the contrast along the shear direction to retrieve the phase  $\varphi$ . In reflection, the phase is related to the surface height  $h$  by  $\varphi = 4\pi h/\lambda$  with the wavelength  $\lambda$  of the light, such that we arrive at

$$h(s) = \frac{\lambda}{4\pi|\Delta|} \int_0^s C_{\text{DIC}} ds' \quad (8)$$

We assumed here that sample is not birefringent and that the phase shift of the reflected light is given by the height of the sample surface only, neglecting internal interfaces. The latter is justified as the green light is absorbed strongly by the structure. The height  $h(s)$  was determined using Eq.(8) with  $s$  along the direction of the shear  $\Delta$ . In the measurements presented in this work we used a UplanFL 20x/0.5NA objective, for which the shear was determined to be  $|\Delta| = 0.55 \mu\text{m}$  using a calibration

slide in transmission DIC consisting of a PMMA pattern of a 200 nm thickness on a glass coverslip, in which case the phase is given by  $\varphi = 2\pi h(n_1 - n_2)$  with the refractive index difference  $n_1 - n_2 = 0.48$  between PMMA and air. To compensate for systematic errors, the measured

$C_{\text{DIC}}$  across the center of the defect was corrected by the  $C_{\text{DIC}}$  along a line displaced perpendicular to the shear, just outside of the defect. An examples of a measured  $C_{\text{DIC}}$  and the resulting height profile  $h(s)$  for defect PD4 are shown in Fig. 14.

- 
- \* Electronic address:ZajacJM@cardiff.ac.uk
- <sup>1</sup> J. Kasprzak, M. Richard, S. Kundermann, A. Baas, P. Jeambrun, J. M. J. Keeling, F. M. Marchetti, M. H. Szymanska, R. Andre, J. L. Staehli, et al., *Nature* **443**, 409 (2006).
  - <sup>2</sup> K. G. Lagoudakis, M. Wouters, M. Richard, A. Baas, I. Carusotto, R. André, D. L. S. Dang, and B. Deveaud-Pledran, *Nature Physics* **4**, 706 (2008).
  - <sup>3</sup> A. Amo, D. Sanvitto, F. P. Laussy, D. Ballarini, E. del Valle, M. D. Martin, A. Lemaitre, J. Bloch, D. N. Krizhanovskii, M. S. Skolnick, et al., *Nature* **457**, 291 (2009).
  - <sup>4</sup> J. M. Zajac, E. Clarke, and W. Langbein, *Applied Physics Letters* **101**, 041114 (pages 4) (2012).
  - <sup>5</sup> M. Abbarchi, C. Diederichs, L. Largeau, V. Ardizzone, O. Mauguin, T. Lecomte, A. Lemaitre, J. Bloch, P. Rousignol, and J. Tignon, *Phys. Rev. B* **85**, 045316 (2012).
  - <sup>6</sup> J. M. Zajac, W. Langbein, M. Hugues, and M. Hopkinson, *Phys. Rev. B* **85**, 165309 (2012).
  - <sup>7</sup> W. Langbein, E. Runge, V. Savona, and R. Zimmermann, *Phys. Rev. Lett.* **89**, 157401 (2002).
  - <sup>8</sup> M. Gurioli, F. Bogani, L. Cavigli, H. Gibbs, G. Khitrova, and D. S. Wiersma, *Phys. Rev. Lett.* **94**, 183901 (2005).
  - <sup>9</sup> D. N. Krizhanovskii, K. G. Lagoudakis, M. Wouters, B. Pietka, R. A. Bradley, K. Guda, D. M. Whittaker, M. S. Skolnick, B. Deveaud-Plaédran, M. Richard, et al., *Phys. Rev. B* **80**, 045317 (2009).
  - <sup>10</sup> N. Chand and S. Chu, *Journal of Crystal Growth* **104**, 485 (1990).
  - <sup>11</sup> K. Fujiwara, K. Kanmoto, Y. Ohta, Y. Tokuda, and T. Nakayama, *Journal of Crustal Growth* **80**, 104 (1987).
  - <sup>12</sup> C. Orme, M. D. Johnson, K. T. Leung, and B. G. Orr, *Material Research Society Symposium Proceedings Vol 340* (1994), ISSN 0921-5107.
  - <sup>13</sup> P. Kreuzer, T. Zacher, W. Naumann, T. Franke, and R. Anton, *Ultramicroscopy* **76**, 107 (1999), ISSN 0304-3991.
  - <sup>14</sup> H. Kawada, S. Shirayone, and K. Takahashi, *Journal of Crystal Growth* **128**, 550 (1993).
  - <sup>15</sup> P. Brunemeier, *J.Vac.Sci.Technol.B* 9(5) p. 2554 (1991).
  - <sup>16</sup> M. Herman and H. Sitter, *Molecular Beam Epitaxy* (Springer-Verlag Berlin, 1989).
  - <sup>17</sup> E. Clarke, private communication.
  - <sup>18</sup> W. Langbein, *Rivista del nuovo cemento* **33**, 255 (2010).
  - <sup>19</sup> L. A. Giannuzzi and F. A. Stevie, eds., *Introduction to focused ion beams: instrumentation, theory, techniques, and practise* (Springer-Verlag Berlin, 2005).
  - <sup>20</sup> M. Abramowitz and I. Stegun, *Handbook of Mathematical Functions: with Formulas, Graphs, and Mathematical Tables* (Dover Publications, 1965).
  - <sup>21</sup> N. McLachlan, *Theory and applications of Mathieu functions* (Oxford, 1947).
  - <sup>22</sup> R. I. Kaitouni, O. E. Daïf, A. Baas, M. Richard, T. Paraiso, P. Lugan, T. Guillet, F. Morier-Genoud, J. D. Ganière, J. L. Staehli, et al., *Phys. Rev. B* **74**, 155311 (2006).
  - <sup>23</sup> H. Waalkens, J. Wiersig, and H. R. Dullin, *Ann. Phys* **260** (1997).
  - <sup>24</sup> R. Coisson, G. Vernizzi, and X. Yang, pp. 3–10 (2009).
  - <sup>25</sup> T. Mano, T. Kuroda, S. Sanguinetti, T. Ochiai, T. Tateno, J. Kim, T. Noda, M. Kawabe, K. Sakoda, G. Kido, et al., *Nano Letters* **5**, 425 (2005).
  - <sup>26</sup> S. Koshiba, Y. Nakamura, M. Tsuchiya, H. Noge, H. Kano, Y. Nagamune, T. Noda, and H. Sakaki, *Journal of Applied Physics* **76**, 4138 (1994).
  - <sup>27</sup> K. Ohta, T. Kojima, and T. Nakagawa, *Journal of Crystal Growth* **95**, 71 (1989), ISSN 0022-0248.
  - <sup>28</sup> D. K. Biegelsen, R. D. Bringans, J. E. Northrup, and L.-E. Swartz, *Phys. Rev. B* **41**, 5701 (1990).
  - <sup>29</sup> T. Liew, I. Shelykh, and G. Malpuech, *Physica E: Low-dimensional Systems and Nanostructures* **43**, 1543 (2011).
  - <sup>30</sup> R. Cerna, D. Sarchi, T. K. Paraiso, G. Nardin, Y. Lèger, M. Richard, B. Pietka, O. E. Daif, F. Morier-Genoud, V. Savona, et al., *Phys. Rev. B* **80**, 121309(R) (2009).
  - <sup>31</sup> V. Mantovani, S. Sanguinetti, M. Guzzi, E. Grilli, M. Gurioli, K. Watanabe, and N. Koguchi, *Journal of Applied Physics* **96**, 4416 (2004).
  - <sup>32</sup> T. Paraiso, M. Wouters, Y. Leger, F. Morier-Genoud, and B. Deveaud-Plédran, *Nature Materials* **9**, 655?660 (2010).